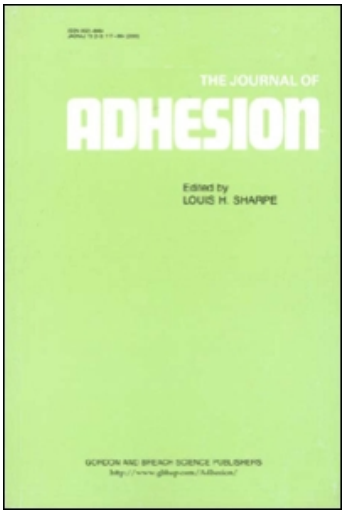

The Journal of Adhesion
Publication details, including instructions for authors and subscription information:
http://www.informaworld.com/smpp/title~content=t713453635

Modelling Environmental Degradation in EA9321-Bonded Joints using a Progressive Damage Failure Model

Y. Hua[a]; A. D. Crocombe[a]; M. A. Wahab[a]; I. A. Ashcroft[b]
[a] School of Engineering, University of Surrey, Guildford, United Kingdom [b] Wolfson School of Mechanical and Manufacturing Engineering, Loughborough University, Loughborough, United Kingdom

To cite this Article Hua, Y. , Crocombe, A. D. , Wahab, M. A. and Ashcroft, I. A.(2006) 'Modelling Environmental Degradation in EA9321-Bonded Joints using a Progressive Damage Failure Model', The Journal of Adhesion, 82: 2, 135 — 160
To link to this Article: DOI: 10.1080/00218460600559557
URL: http://dx.doi.org/10.1080/00218460600559557

The Journal of Adhesion, 82:135–160, 2006

ISSN: 0021-8464 print/1545-5823 online
DOI: 10.1080/00218460600559557

Taylor & Francis
Taylor & Francis Group

Modelling Environmental Degradation in EA9321-Bonded Joints using a Progressive Damage Failure Model

Y. Hua
A. D. Crocombe
M. A. Wahab
School of Engineering, University of Surrey, Guildford, United Kingdom

I. A. Ashcroft
Wolfson School of Mechanical and Manufacturing Engineering, Loughborough University, Loughborough, United Kingdom

A progressive cohesive failure model has been proposed to predict the residual strength of adhesively bonded joints using a moisture-dependent critical equivalent plastic strain for the adhesive. Joints bonded with a ductile adhesive (EA9321) were studied for a range of environmental degradations. A single, moisture-dependent failure parameter, the critical strain, was calibrated using an aged, mixed-mode flexure (MMF) test. The mesh dependence of this parameter was also investigated. The parameter was then used without further modification to model failure in aluminum and composite single-lap joints (SLJ) bonded with the same adhesive. The FEA package ABAQUS was used to implement the coupled mechanical-diffusion analyses required. The elastic–plastic response of the adhesive and the substrates, both obtained from the bulk tensile tests, were incorporated. Both two-dimensional and three-dimensional modelling was undertaken and the results compared. The predicted joint residual strengths agreed well with the corresponding experimental data, and the damage propagation pattern in the adhesive was also predicted correctly. This cohesive failure model provides a simple but reliable method to model environmental degradation in ductile adhesive bonded joints, where failure is predominantly within the adhesive layer.

Keywords: Cohesive failure; Coupled; Environmental degradation; Mechanical-diffusion analyses; Nonlinear finite element analysis; Progressive damage; Single-lap joints

Received 12 August 2005; in final form 19 December 2005.

Address correspondence to A. D. Crocombe, School of Engineering (H5), University of Surrey, Guildford, Surrey, GU2 7XH, UK. E-mail: a.crocombe@surrey.ac.uk

INTRODUCTION

Adhesives offer numerous benefits compared with alternative joining methods. These benefits include improved impact resistance, structural integrity, enhanced aesthetics, simplified assembly, increased corrosion resistance, reduced manufacturing costs, weight savings, and the ability to join different materials. They are used in the automotive, aerospace, electronic, and packaging industries.

Some of the main restrictions to a more widespread use of adhesives has been that the lifetime of bonded joints are difficult to model accurately and their long-term performance cannot easily and reliably be predicted, especially under the combined effects of an aggressive environment and mechanical loading. A commonly encountered hostile environment is exposure to moisture, often at elevated temperatures. The problem of durability of adhesive joints in hostile environments has become the main challenge for the researchers in this area.

Many kinds of experimental techniques have been undertaken to study the durability of adhesively bonded joints. It has been found that the degradation of the bonded joint depends on the type of substrate and adhesive, the type of surface pretreatment, the loading configuration, and the ageing environment [1]. Two main types of failure, interfacial and cohesive, are commonly found for adhesive joints: failure sites are at the adhesive/substrate interface or cohesive within the adhesive, respectively.

A predictive modelling methodology can help reduce the uncertainty in the residual strength after prolonged service. Finite element analysis (FEA) has been employed to develop durability prediction models based on progressive failure analysis [2–5]. This work has focused on material separation modelling using a predefined crack-propagation path and an interfacial rupture element. Such an approach is known as cohesive zone modelling (CZM). However, modelling progressive cohesive failure, where failure is mainly within the adhesive layer, has achieved much less attention. A predictive cohesive failure modelling methodology has been proposed and demonstrated in this article to improve this situation.

BACKGROUND

To deal with general progressive ductile material failure, several kinds of methods have been developed. Amongst these are the virtual internal bond (VIB) model, the porosity-based Gurson model, the continuum damage mechanics (CDM) model, and the simple, strain-based cohesive failure model. These approaches have recently attracted the

attention of a number of researchers, mainly because of the variety of practical applications where traditional fracture mechanics concepts have reached their limitations.

The VIB model has recently been proposed by Gao *et al*. [6, 7] wherein the constitutive model directly incorporates a cohesive-type law without a separate fracture criterion. In this model, the continuum nature of the materials is treated as a random network of material points which are interconnected by a number of bonds controlled by a cohesive law. The bonds are physically described by a bond energy–bond length relation. The derivative of the energy with respect to the bond length provides the cohesive bond force. Most recently, an approach to incorporating plastic deformation into the VIB model has been presented and discussed [8, 9]. The incorporation of plasticity/viscoplasticity at the continuum level is done within the framework of the multiplicative decomposition of the deformation gradient as proposed by Lee [10].

It has been pointed out that this method differs from an atomistic model in that a phenomenological "cohesive force law" is assumed to act between "material particles" which are not necessarily atoms. However, the most accurate solution obtainable using a VIB material model occurs when the element sizes, and even the element shapes, correspond directly with the underlying microstructure of the actual material. Therefore, this model appears less suitable for the simulation of fracture in large-scale structures than in small-scale ones because of the presence of strains above levels typically found in macroscopically sized structures. That means the contribution to the work to fracture in these structures becomes dependent on size and geometry [8]. Another difficulty is that ill-posedness in the elliptic region implies very severe instability of the discrete system, and numerical methods can fail with such instability [9].

The Gurson model [11] is a microvoid damage-accumulation model used to study cohesive failure of ductile materials in a porosity-based way. It was proposed to model ductile fracture of metal by considering the growth of a single void in an ideal elastoplastic matrix. An essential feature of this material model is that a failure criterion is directly built into the constitutive equations and, thus, when the void volume fraction approaches a critical value, the material locally loses its stress-carrying capacity. To account for the effects of void nucleation and coalescence observed in experiments, the original Gurson model was modified and extended into a semiphenomenological form by Needleman and his coworkers [12–15]. Most recently, a number of nonlocal extensions [16] of Gurson-based local models have been proposed to minimise the localisation of the damage process at a material

point and the finite-element mesh effects caused when using such local models.

However, the Gurson model in its general form requires the determination of a large number of parameters. Some can be estimated on the basis of metallurgical observations, as for the case of the volume fraction of voids associated with the nucleated particles. The remaining porosity parameters have to be determined with the help of numerical and experimental procedures [17]. As an alternative to the tensile specimen geometry, compact tension data have been used to calibrate the Gurson parameters. However, these geometries require a model capable of quantifying the effects of triaxiality on porosity evolution. Even the minimum number of independent experimental tests necessary to identify the parameters for Gurson models becomes very large for a modified constitutive model [18]. Moreover, all the parameters calibrated are not directly related to physical quantities even though they can describe the effects related to the evolution of the microcavities quite well. Finally, it is important to mention that Gurson models can suffer from mesh and scale effects. Some nonlocal Gurson methods have been proposed to solve this problem but have made the calibration procedures even more complicated [18].

As an alternative to the porosity-based approach, Lemaitre [19] and Lemaitre and Chaboche [20] proposed a constitutive framework for ductile failure processes known as the continuum damage mechanics (CDM) method. This model differs from the porosity-based Gurson model because, in the CDM model, damage is one of the state variables, and this variable takes into account the microstructural changes. The damage process that occurs in a reference volume element (RVE) while plastic deformation takes place is described by the global effects that all damage phenomena have on the RVE constitutive response. As with the Gurson models, the damage parameters of the CDM model have to be calibrated using experimental data before the model can be implemented in the FE simulation. However, the number of the parameters is much smaller than those required by a Gurson model. It is also worth noting that in a CDM model the parameters have a physical meaning and can be experimentally determined without the need for iterative calculations. However, the CDM model is a local model, and it does not account for size and geometry effects, which can restrict its use as a general continuum damage-modelling method [21].

In this research, a strain-based cohesive failure model is used. This is the simplest method of modelling progressive continuum failure within FE analysis. Material follows the nonlinear constitutive response until the maximum equivalent plastic strain reaches a

critical value at any element integration point. An element with all the nodes in excess of this critical strain will fail. The failed elements form a natural failure-propagation path in the model. This model has been used not only to predict the failure load of the joints but also to study the damage initiation and propagation. The only parameter required is the critical maximum strain, which is obtained from mixed-mode flexure calibration tests at different levels of moisture concentration. One problem with this method is the mesh dependence, observed when analysing configurations with singular stress fields. This aspect is discussed later.

A coupled diffusion-mechanical analysis was implemented in the commercial finite-element package ABAQUS. It was necessary to measure and characterise the moisture-uptake behaviour of the adhesive during ageing. Although no universal diffusion model is available, analytical solutions of moisture diffusion have been developed based on Fick's law [22] and are widely used in modelling the diffusion in adhesively bonded structures. The mechanical analysis includes moisture-dependent constitutive data for the adhesive. Numerous test methods have been developed to characterise the moisture-dependent mechanical properties of the adhesive, from bulk adhesive specimens to specially designed bonded joints such as the thick adherend shear test (TAST). In this work bulk tensile specimens have been used.

EXPERIMENTAL METHODOLOGY AND MATERIALS CHARACTERISATION

Hysol EA9321 (Henkel Aerospace, Bay Point, CA, USA) is a two-component thixotropic paste adhesive, which exhibits toughness, retains strength at elevated temperatures, and yields durable bonds over a wide temperature range. Bulk film samples were manufactured and cured at room temperature for 7 days before being exposed in an artificial ageing environment of 95.8% RH at an ageing temperature 50°C as stated in ASTM E104 [23] or BS 3718. To manufacture void-free films, the adhesive had to be mixed under vacuum, breaking the bubbles to release the trapped air. After the air has been released, the adhesive was placed between release films and compressed between thick glass plates. The final thickness was controlled by spacers. A digital hygrometer was used to ensure the required environment was maintained. The moisture-uptake performance of EA9321 was determined using a gravimetric approach. Specimens were periodically removed from the ageing environment, surface water was removed using analytical-grade tissue paper, and the specimen was weighed using a Mettler M5 analytical microbalance.

TABLE 1 Fickian Diffusion Data for 0.48-mm-thick EA9321

Parameter	Value
Ageing environment	95.8% RH, 50°C
Diffusion coefficient (m^2/s)	3.0×10^{-13}
Equilibrium mass uptake (m_∞)	3.85%

It was found that the response for the 0.48-mm-thick film was fitted well by the Fickian model given in Equation (1). The diffusion coefficient (D) and the equilibrium mass uptake (m_∞) are listed in Table 1. The predicted results are shown in Figure 1 together with the experimental data.

$$\frac{mwt_t}{mwt_\infty} = 1 - \frac{8}{\pi^2}\sum_{n=0}^{\infty}\frac{1}{(2n+1)^2}\exp\left[\frac{-D(2n+1)^2\pi^2 t}{4l^2}\right]. \quad (1)$$

The moisture-dependent mechanical properties of environmentally aged bulk EA9321 were determined using uniaxial tension tests with adhesive film dogbone specimens. Experimental stress–strain curves for 0.48-mm-thick EA9321, obtained from the dry specimens and the 95.8% RH aged specimens (giving a moisture saturation value of 3.85%) are shown in Figure 2. These data were used for the subsequent durability modelling of the mixed-mode flexure (MMF)

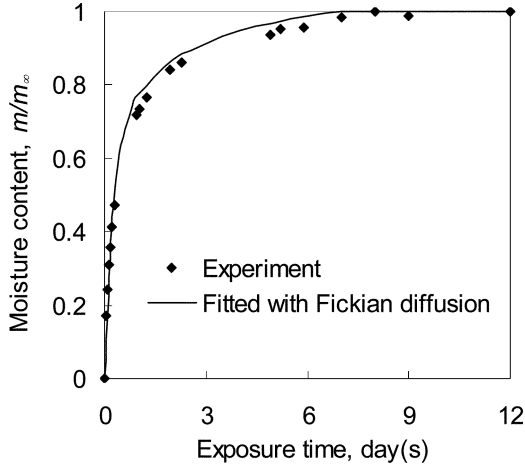

FIGURE 1 Experimental data fitted with Fickian diffusion for 0.48-mm-thick EA9321 adhesive film (95.8% RH, 50°C).

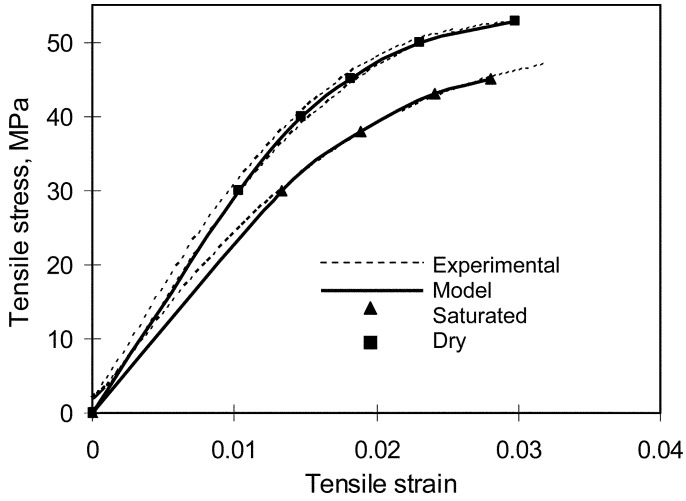

FIGURE 2 Moisture-dependent tensile constitutive properties of bulk EA9321 (saturated moisture concentration $m_\infty = 3.85\%$).

and single-lap joint (SLJ) tests. The material behavior of EA9321 at an intermediate moisture level was determined by linear interpolation between results from the dry and the saturated conditions.

The MMF configuration, shown in Figure 3, has been chosen to calibrate the moisture-dependent critical strain parameter of the adhesive. It is a significantly different configuration from the SLJ specimens tested later and, hence, a good test of the general applicability of the cohesive failure model. The specimen consists of aluminum alloy 7075-T6 substrates bonded with a 0.5-mm-thick EA9321 adhesive

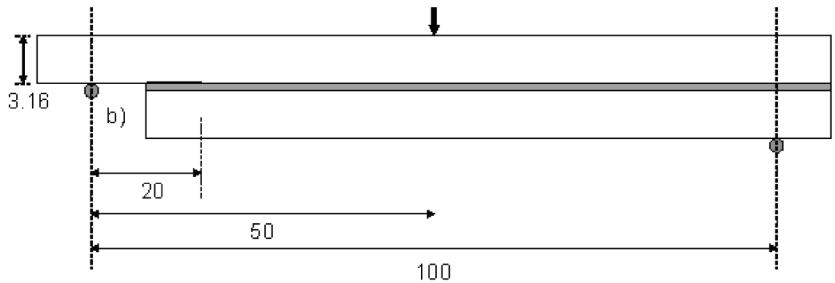

FIGURE 3 Geometry and loading configuration of the MMF specimen, all dimensions in millimeters (width 12.7 mm).

layer. The adhesive was cured on the upper substrate, and this was exposed in different environments before a secondary bond was used to attach the lower substrate and complete the specimen. Two moisture saturation levels were achieved for the MMF specimens: 2.1% at 70°C/79.5% RH and 3.85% at 50°C/95.8% RH. The thicknesses of the MMF substrates (3.16 mm) were sufficient to prevent their yielding during testing. A 20-mm precrack was introduced on the EA9321 adhesive–aluminum interface using a teflon film. The specimens were loaded in three-point bending at a displacement rate of 0.05 mm/min, and the crack length corresponding to the fracture load was measured using an *in situ* video microscope. The fracture loads recorded for the MMF tests were used in conjunction with the FEA modelling to determine the moisture-dependent critical strain of the adhesive. The failure loads at different crack lengths for the MMF tests are shown in Figure 4. The MMF-calibrated strain has then been used directly to predict the failure loads of the same adhesive system but in a single-lap joint configuration with different substrates.

The two single-lap joints configurations of EA9321 studied are shown in Figure 5(a) and (b). The substrates were aluminum alloy 7075-T6 [Figure 5(a)] and the unidirectional carbon fibre epoxy composite IM7-8552 [Figure 5(b)]. The fillet size at both lap ends was about 0.62 mm/0.90 mm by radius (r)/chord (c) as illustrated

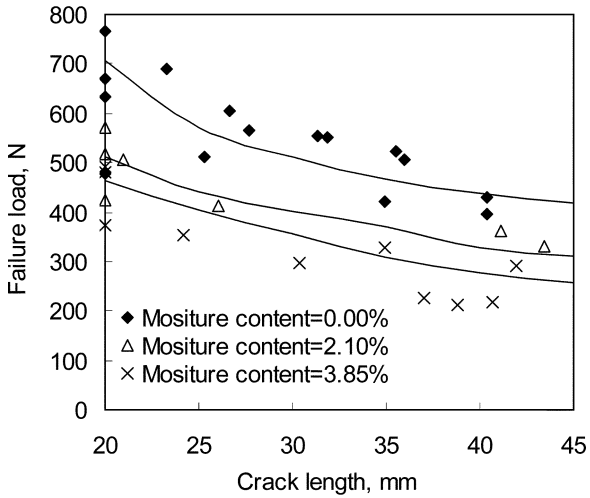

FIGURE 4 Experimental failure load of MMF joints at different crack lengths (markers) and predicted failure load of MMF specimens using the calibrated failure strain (lines).

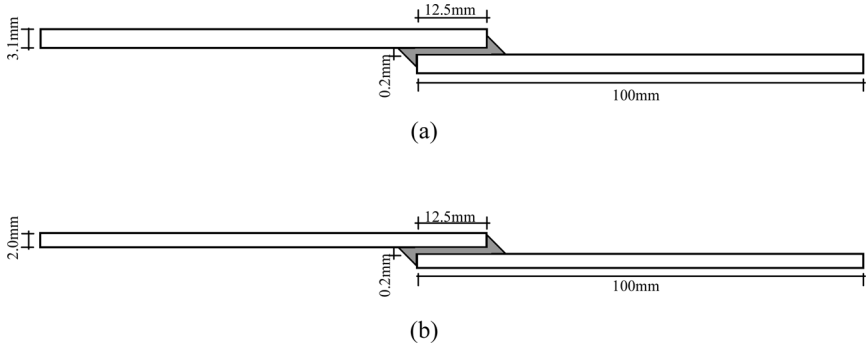

FIGURE 5 (a) EA9321/7075-T6 single-lap joint geometry (not to scale); (b) EA9321/IM7-8552 single-lap joint geometry (not to scale).

in Figure 6. The material properties of 7075-T6 and IM7-8552 obtained from the standard tests, Refs. [24] and [25], are shown in Figure 7 and Table 2, respectively. The bondline thickness of the adhesive in the EA9321/aluminum joints was controlled to 0.2 mm ± 15%, and the bondline thickness of the EA9321/composite joints was 0.2 mm ± 20%. The joints were aged at 50°C, 95.8% RH for intervals of 0, 2, 4, 8, 12 (or 16), and 26 weeks before being withdrawn for testing. Five specimens of the EA9321/aluminum joints and three specimens of the EA9321/composite joints were tested for each withdrawal. The tests were carried out under ambient conditions at a constant displacement rate of 1 mm/min. It was found that the failure of the EA9321/aluminum joints were all primarily cohesive in the adhesive near to the interface, and the failure of the EA9321/composite joints were a combination of cohesive failure in the adhesive close to interface and delamination of the substrate. These experimental results were used to validate the prediction of the cohesive failure model using FEA modelling.

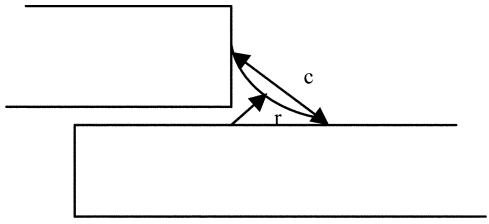

FIGURE 6 Fillet configuration of the EA9321-bonded SLJs (not to scale).

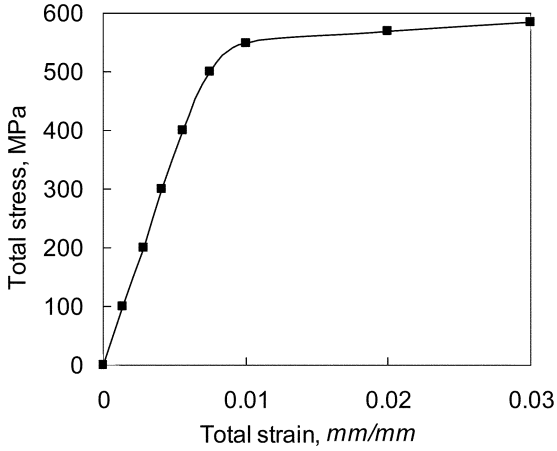

FIGURE 7 Aluminum 7075-T6 tensile stress–strain curve ($E = 72\,\text{GPa}$, $v = 0.33$).

PROGRESSIVE DAMAGE MODELLING OVERVIEW

Cohesive failure is often found in well-made joints bonded with ductile adhesives such as EA9321. It is often difficult to locate the damage initiation point and propagation path. The failure model coded within ABAQUS [26] can not only predict the strength but also the damage initiation and propagation within an adhesive joint. To describe accurately the stress and strain distribution in the adhesive, the experimental moisture-dependent elastic–plastic material properties of the adhesive were incorporated into the model, using von Mises yielding. Then a critical maximum equivalent plastic strain failure criterion was added to restrict the stress-carrying capability of the elements as shown in Figure 8.

When an element integration point reached this predefined critical strain, it failed and lost its load-carrying capacity. An element failed when all its integration points failed and showed as a void in the mesh of the model. The stress that was carried by this element was redistributed to the adjacent elements, and the damage propagated.

TABLE 2 IM7-8552 Mechanical Properties used for Modelling

E_{11} [GPa]	E_{22} [GPa]	E_{33} [GPa]	G_{12} [GPa]	G_{13} [GPa]	G_{32} [GPa]	ν_{12}	ν_{13}	ν_{32}
160	10	10	4.8	4.8	3.2	0.31	0.31	0.52

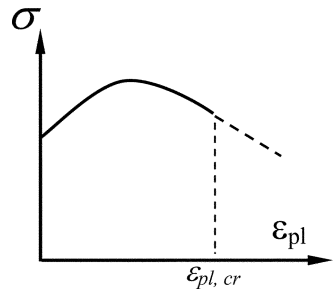

FIGURE 8 Cohesive failure model limited by the critical strain $\varepsilon_{pl,or}$.

The whole joint failed once a path of failed elements extended over the entire overlap. The residual strength is the maximum load carried by the joint. The MMF configuration shown in Figure 3 was used to calibrate this parameter at various moisture levels and then this moisture-dependent calibrated failure strain was used for predictive modelling of the SLJs shown in Figures 4 and 5.

MMF CALIBRATION OF THE CRITICAL STRAIN

A FE model of the MMF joint with elements in the adhesive layer of 0.05 mm × 0.05 mm was created and is shown in Figure 9. Plane strain four-noded quadrilateral elements were used. The moisture-dependent material property of the adhesive was calculated using linear interpolation between the dry and saturated data shown in Figure 1.

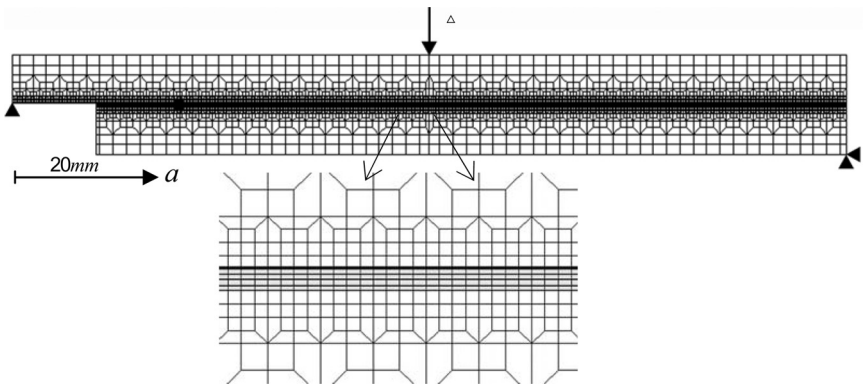

FIGURE 9 MMF finite-element model with mesh refinement along the adhesive overlap.

Explicit analysis has to be used when implementing the cohesive failure model in ABAQUS [26]. A mass scaling factor of 1×10^5 was used to prevent dynamic instability. This value provided a time-efficient solution but did not modify the accuracy of the static analyses. Nonlinear geometric behavior was included in the modelling. Three moisture concentration levels (dry, 2.1%, and 3.85%) were considered, and the calibrated results for the MMF strength as a function of moisture uptake, normalised by the saturation value $m_\infty = 3.85\%$, is shown in Figure 10. It can be seen that the failure strain reduces with moisture content. This is not apparent in the adhesive tensile data presented in Figure 2. From both the MMF and the SLJs discussed later, there is evidence that the failure, although still mainly cohesive, shifted towards the interface. Thus, it is conjectured that in a joint the wet adhesive fails at a strain below the value measured in the bulk tensile testing, shown in Figure 2. The reason for this is not certain, but one possibility is that the adhesive at the interface was degraded preferentially; maybe the molecular structure adjacent to the interface was more susceptible to moisture.

As expected, it was found that the moisture-dependent critical strain was also mesh dependent. The calibrated results for different mesh schemes for the dry condition are shown in Figure 11(a).

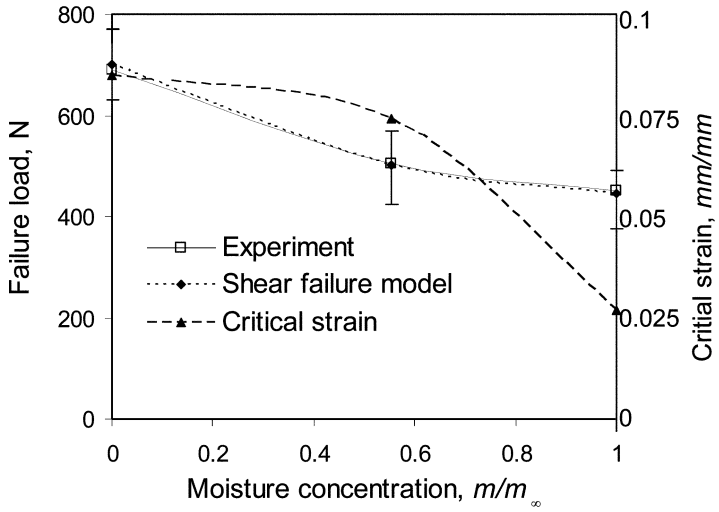

FIGURE 10 Critical strain calibration for MMF specimens at different moisture concentration levels (smallest mesh size $0.05\,\text{mm} \times 0.05\,\text{mm}$, $m_\infty = 3.85\%$).

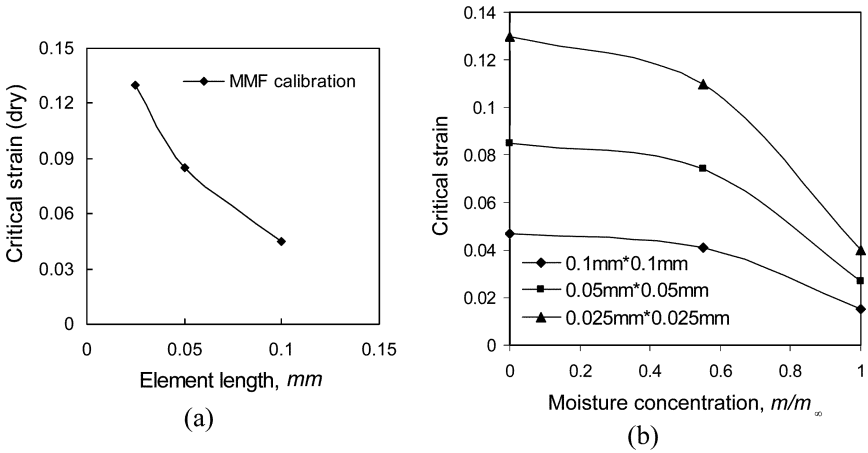

FIGURE 11 Critical strain calibration for MMF specimens at different moisture concentration levels for different mesh schemes ($m_\infty = 3.85\%$): (a) undegraded; (b) degraded.

This mesh dependence clearly arose from the singularity existing around the embedded bimaterial corner. If both the failure strain and the crack opening displacement were known, then it would be possible to determine and use a "characteristic length" for the elements. This is not the case here, and so three different element sizes have been used. Figure 11(a) shows that the failure strains effectively follow the inverse relationship with element size as required by the principle of "characteristic lengths." Further study has found that there was a proportional relationship for the calibrated failure strain between the different mesh schemes at each moisture concentration level, as illustrated in Equation (2):

$$\epsilon^1_{c,m}/\epsilon^2_{c,m} = \epsilon^1_{c,\mathrm{dry}}/\epsilon^2_{c,\mathrm{dry}} \tag{2}$$

Much modelling and computation work for the cohesive failure model can be saved by using Equation (2) where the superscript numbers 1 and 2 denote different mesh schemes. The moisture-dependent critical strain calibration results of the MMF specimens for the three different mesh schemes are shown in Figure 11(b). These values were used to model cohesive failure in the single-lap joints bonded by the same adhesive without further modification. This failure modelling approach can be used with other meshes and even other materials as long as the failure strain appropriate to the mesh size is used. The failure strain can be linked with the mesh size either by calibration

from another joint (as in this work) or from basic material data. To avoid multiple analyses with different meshes, an inverse relationship may be assumed between the mesh size and the failure strain.

PREDICTIVE MODELLING OF THE SINGLE-LAP JOINTS USING THE COHESIVE FAILURE MODEL

The single-lap joint is the most common test method used to evaluate the strength of an adhesive joint. The two different joint configurations used are shown in Figures 4 and 5.

EA9321/Aluminum SLJ

The EA9321/aluminum single-lap joint shown in Figure 5(a) was considered first. Because of the symmetry of the SLJ configuration, only half the joint was modelled. The modelling was used to predict the residual strength of the joints after exposure to moisture. The mesh was generated using plane strain four-noded quadrilateral elements with an element size of 0.05 mm in the adhesive layer, as shown in Figure 12. Rotational symmetry was applied to a section through the middle of the overlap, also shown in Figure 5(a). The degradation was assumed to be the same from both ends of the lap region. The same moisture-dependent stress–strain curves and critical failure strains calibrated from the MMF modelling were used for the SLJ

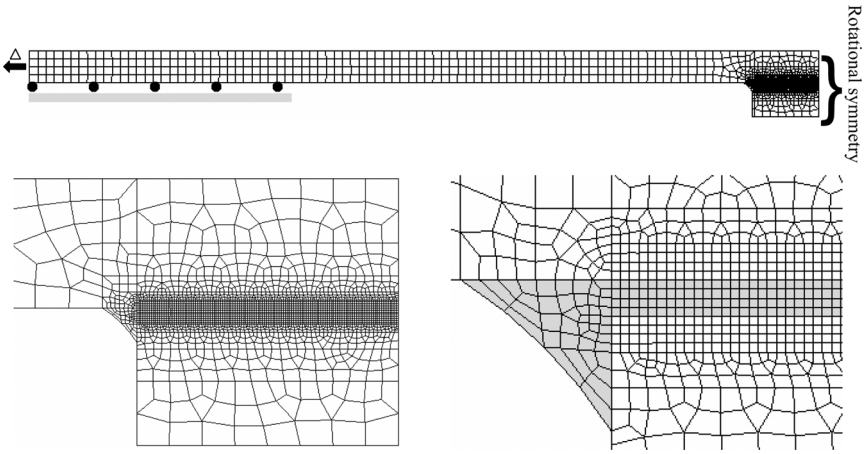

FIGURE 12 FE model of the EA9321/aluminum SLJ and local mesh refinement (smallest mesh size: 0.05 mm × 0.05 mm).

modelling. As with the MMF analysis, explicit analysis was applied with a mass scaling factor of 1×1^5, and geometric nonlinearity was taken into account.

Standard Fickian diffusion was used to obtain the moisture profiles along the overlap length. The mass diffusion model coded in ABAQUS [26] was used to generate the normalised nodal moisture concentration as field output for the coupled diffusion–mechanical analysis. The diffusion parameters were as shown in Table 1. The moisture distributions in the adhesive layer after exposure to moisture for 2, 8, and 26 weeks are shown in Figure 13.

The critical strain–moisture concentration curves previously calibrated from the MMF modelling for the three mesh schemes were used as the failure parameters for the SLJ models. The variation of the residual strengths of the joint obtained from the experimental results and the finite-element modelling with time of exposure is shown in Figure 14, and the full dataset is also presented in Table 3. The testing was carried out by partners at MBDA (MBDA Ltd., Stevenage, UK) and four or five replicates were used for each ageing time. It can be seen in Figure 14 that the finite-element modelling predictions for the three different mesh schemes agreed well with the experimental results. Thus, the use of mesh-dependent failure parameters successfully dealt with the mesh sensitivity of the adhesive stress and strain values. The experimental data exhibited considerable scatter at the

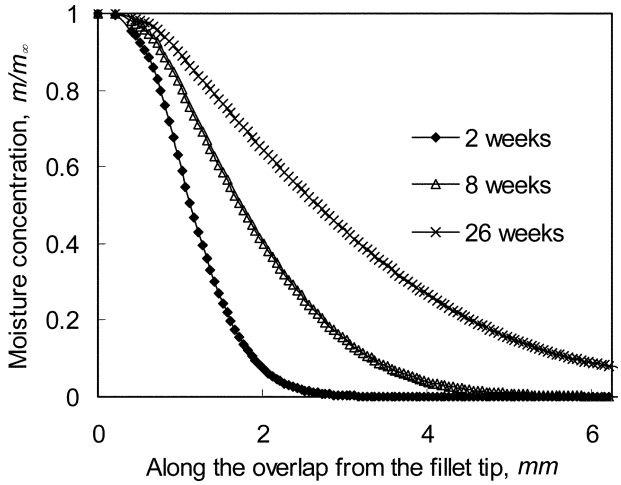

FIGURE 13 Normalised moisture distribution profile in the adhesive layer of the EA9321/aluminum joint after exposure to moisture for 2, 8, and 26 weeks.

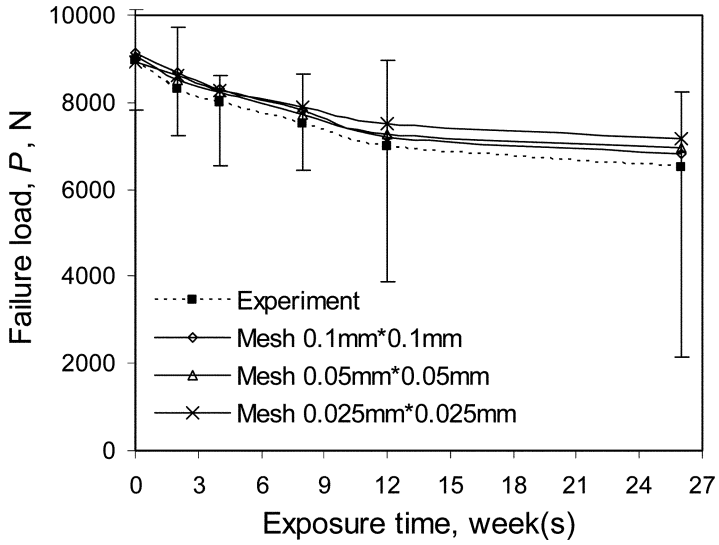

FIGURE 14 Predicted ultimate failure load of the EA9321/aluminum SLJ using the cohesive failure model.

longer exposure times. There were specific outlying data at 12 weeks (4.4 kN) and 26 weeks (2.3 kN). There was some evidence to suggest that these lower strengths may not have been representative and this then would reduce the scatter and further enhance the correlation between the predicted and measured strengths.

Another advantage of this continuum modelling method is that the cohesive damage initiation and propagation within the adhesive layer can also be predicted. A series of contour plots selected from the 26-week degraded-joint model with the mesh scheme of 0.05 mm $\times$ 0.05 mm are shown in Figure 15. The failed elements have been marked in white. These show visually the damage-propagation

TABLE 3 Experimental Failure Loads of the Aluminium Single-Lap Joints

Exposure, wk	Load, N					
0	10276	9798	8658	8570	8440	7996
2	9586	9373	7953	7193	7366	
4	8724	7439	8341	8439	6952	
8	7773	6590	7380	8353		
12	7394	7739	8412	4379		
26	8195	7964	8011	5968	2313	

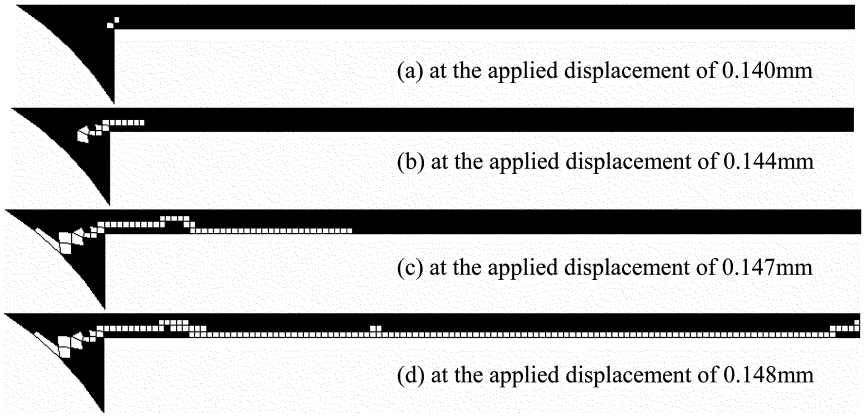

FIGURE 15 Damage propagation in the EA9321/aluminum SLJ model (26 weeks degraded, smallest mesh size 0.05 mm × 0.05 mm).

trail with an increase of the applied displacement. The damage initiated around the corner of the joint, propagated first along the centre of the adhesive for a short distance (and through the fillet), and then extended mainly along the lower interface of the adhesive layer to the middle of the joint. This failure pattern has been observed in the tested specimens. It is worth noting that this damage location appeared to be insensitive to the mesh refinement. The complete damage contour trails for a 0.1 mm × 0.1 mm mesh model and a 0.025 mm × 0.025 mm mesh model are illustrated in Figure 16. Two graphs of the predicted loading history and damage-propagation progress obtained from an undegraded joint model and a 26-week degraded-joint model with the 0.05 mm × 0.05 mm mesh are shown in Figure 17.

The load in the undegraded specimen increased linearly with applied displacement and peaked at about 9.14 kN before suddenly

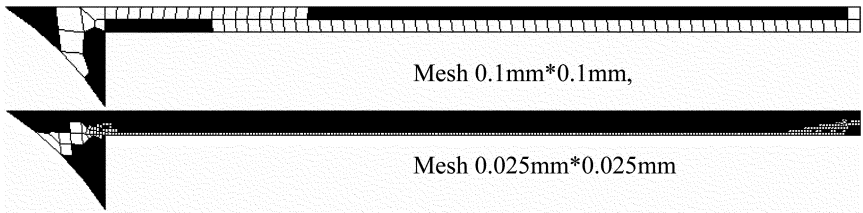

FIGURE 16 Damage location in the SLJ models using the cohesive failure model (EA9321/aluminum SLJ model, 26 weeks degraded).

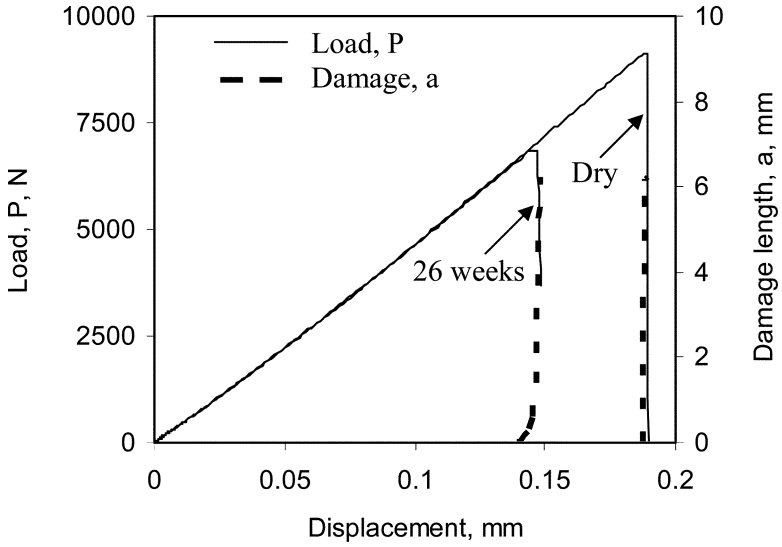

FIGURE 17 Predicted loading history and damage propagation in an undegraded joint and a joint aged for 26 weeks (EA9321/aluminum SLJ model, smallest mesh size 0.05 mm × 0.05 mm).

failing. The damage in the adhesive initiated and propagated very quickly. The predicted loading history of the 26-week degraded joint gave a similarly linear loading increase and a catastrophic drop. However, there was a degree of nonlinearity close to the end in both the loading history and the damage-propagation process. In this degraded model, the damage initiated at an applied displacement level of 0.140 mm and extended over 2.1 mm as the applied displacement increased. Failure then went though the rest of the adhesive layer as the joint reached the ultimate load.

EA9321/Composite SLJ

A finite-element model of the EA9321/composite single-lap joint was also generated for cohesive failure analysis. Again, a half mesh model was designed using four-noded quadrilateral elements with mesh refinement around the lap region as shown in Figure 18. A rotational boundary condition was specified at the line of symmetry, and displacement loading was applied at the end. The size of the adhesive elements in the overlap were 0.05 mm × 0.05 mm, giving a total of four rows of elements across the 0.2 mm-thick adhesive layer. The moisture-dependent mechanical property of EA9321 shown in Figure 2

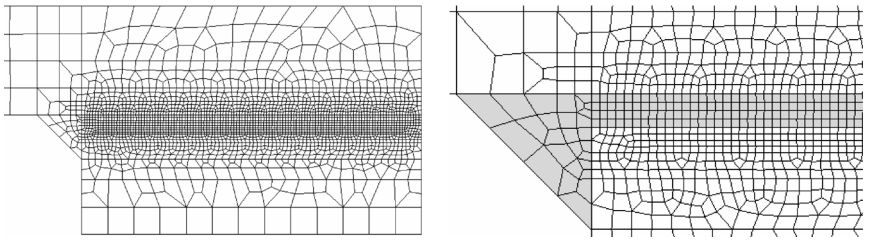

FIGURE 18 FE model of the EA9321/composite SLJ and local mesh refinement (smallest mesh size: 0.05 mm × 0.05 mm).

and the orthotropic composite data shown in Table 2 were assigned to the adhesive and the substrates, respectively. The same moisture-dependent critical strain calibrated from the MMF analyses was used for failure modelling in the joint.

The same standard Fickian diffusion model was used to specify the moisture diffusion from one end of the lap region towards the line of symmetry. However, moisture can also diffuse through the composite substrates. The Fickian diffusion parameters for the composite, obtained from our coworkers, are shown in Table 4. To study the effect of the moisture diffusion through the substrate on the moisture distribution in the adhesive layer, two diffusion schemes, m1 and m2 (with and without composite diffusion, respectively) were used. The resulting moisture distributions along the adhesive layer are compared in Figure 19. It was found that the increase of moisture concentration in the adhesive with the substrates modelled as permeable was significantly accelerated at extended exposure times. The average moisture concentration in the adhesive was increased by about 20% after the joint has been exposed for 4 weeks and by about 80% following 26 weeks' exposure. The predicted residual strengths of the EA9321/composite joint for the two moisture-diffusion schemes are shown in Figure 20. The reduction of the residual strength for the joint degraded for 26 weeks was about 10%. The experimental results are also shown in Figure 20 and compared with the finite-element

TABLE 4 Fickian Diffusion Data for IM7-8552 Unidirectional CFRP

Moisture environment	D-parallel to fibre axis (m^2/s)	D-perpendicular to fibre axis (m^2/s)	Equilibrium mass uptake (%mwt_∞)
95.8% RH, 50°C	7×10^{-13}	2×10^{-13}	~1.0

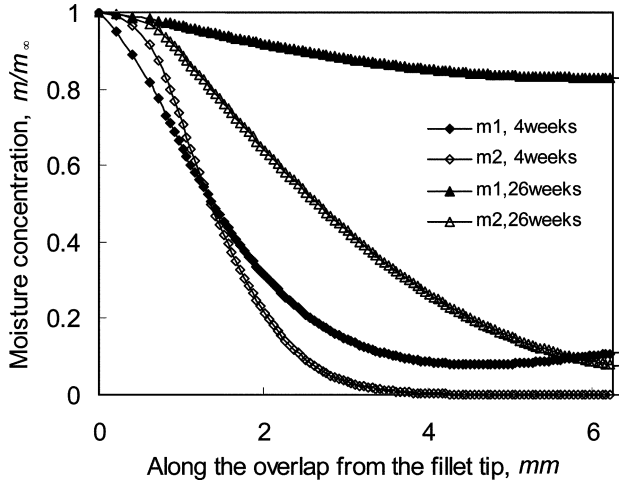

FIGURE 19 Moisture distribution profile in the SLJ adhesive layer from the diffusion analysis m1 and m2 (with and without the composite moisture diffusion).

predictions. The full dataset is shown in Table 5. Testing was again carried out by our project partners at MBDA, and three or four replicates were tested for each exposure time.

The predicted residual strengths matched the experimental results quite well except at intermediate ageing times. The prediction of the degraded joints based on the composite diffusion scheme was closer to the experimental solution than the model excluding the substrate diffusion. However, both were still higher than the experimental results. This was probably due to the absence of the composite failure in the modelling, although some delamination of the substrates did occur in the joints tested.

3D Modelling of the SLJ

The predicted residual strength and damage propagation of the single-lap joint has been determined as a function of the ageing time. However, the previous finite-element modelling was all two-dimensional (2D) including the moisture-diffusion analysis of the SLJ specimens. This has excluded the third direction of moisture penetration, and therefore, has not given a complete simulation of the moisture profile. To achieve this, a three-dimensional (3D) coupled diffusion-stress FE model was developed and is discussed in this section.

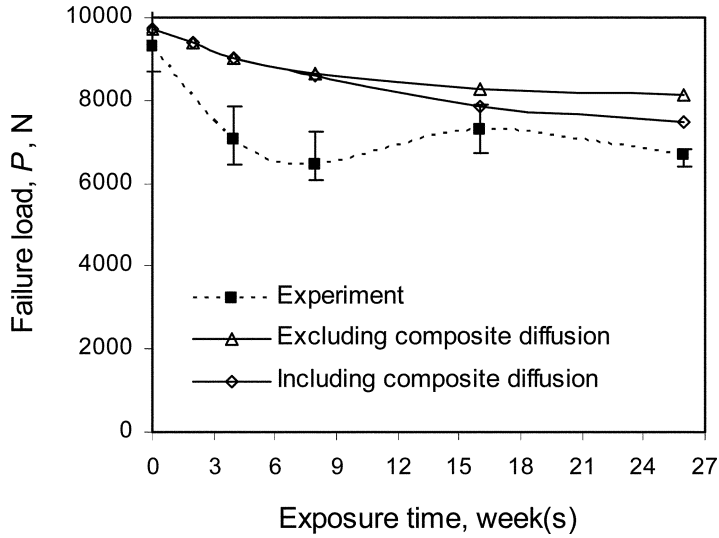

FIGURE 20 Predicted ultimate failure load of the EA9321/composite SLJ using the cohesive failure model for the different composite diffusion schemes (smallest mesh size 0.05 mm × 0.05 mm).

A 3D MMF model has been created, and the moisture-dependent critical strains shown in Figure 11 were used for strength predictions. It was found that the predicted MMF joint strengths were only slightly higher (2–3%) than the strengths predicted from the 2D modelling. Thus, the same moisture-dependent critical strains were used in the 3D modelling of the SLJs. A 3D finite-element model of a quarter of the EA9321/aluminum single-lap joint is shown in Figure 21. The maximum and the minimum mesh sizes were 0.75 mm × 0.75 mm × 0.5 mm and 0.1 mm × 0.1 mm × 0.5 mm, respectively. The full diffusion path was considered, as shown in Figure 22.

TABLE 5 Experimental Failure Loads of the CFRP Single-Lap Joints

Exposure, wk	Load, N			
0	10240	9188	9036	8775
4	6619	6697	7896	
8	5931	6918	6526	
16	7228	7029	7634	
26	6255	6968	6848	

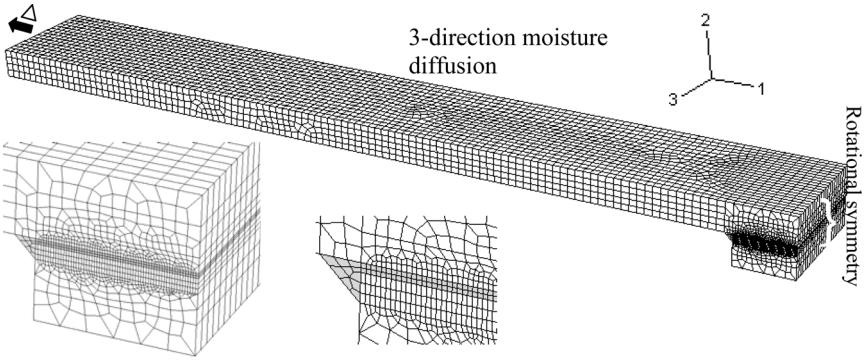

FIGURE 21 3D quarter model of the EA9321/aluminum SLJ and local mesh refinement (smallest mesh size 0.1 mm × 0.1 mm × 0.5 mm).

The predicted moisture distribution profile from the joint degraded for 26 weeks is shown in Figure 22.

In the 2D model, moisture only diffuses in the 1-direction, so that any section along the adhesive width had the same moisture profile. It can be seen in the 3D model that the moisture diffusion in the adhesive layer flowed from both the 1- and 3-directions. A reduction in the predicted failure load using the 3D model was expected. However, because the adhesive width was twice the adhesive length, the 1-direction diffusion was the main contributor to the moisture profile. Thus, the reduction in the modelling results was relatively modest. The predicted residual strengths from the 2D and the 3D model of the joint after being exposed for 26 weeks are compared in Figure 23. The failure-load reduction from the 2D model to the 3D model was around 8%. The predicted stiffness was also reduced from

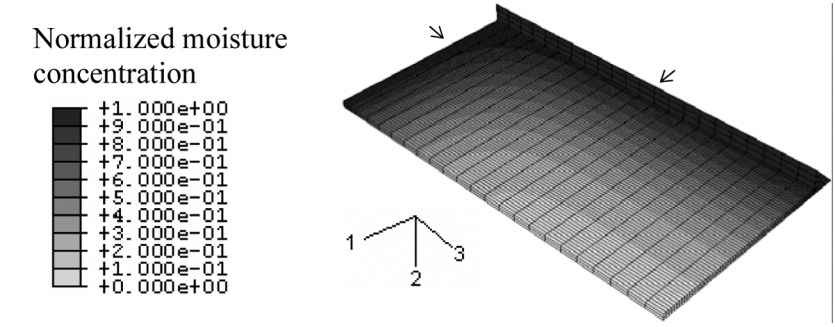

FIGURE 22 Adhesive moisture profile in the EA9321/aluminum SLJ specimen aged for 26 weeks (smallest mesh size: 0.1 mm × 0.1 mm × 0.5 mm).

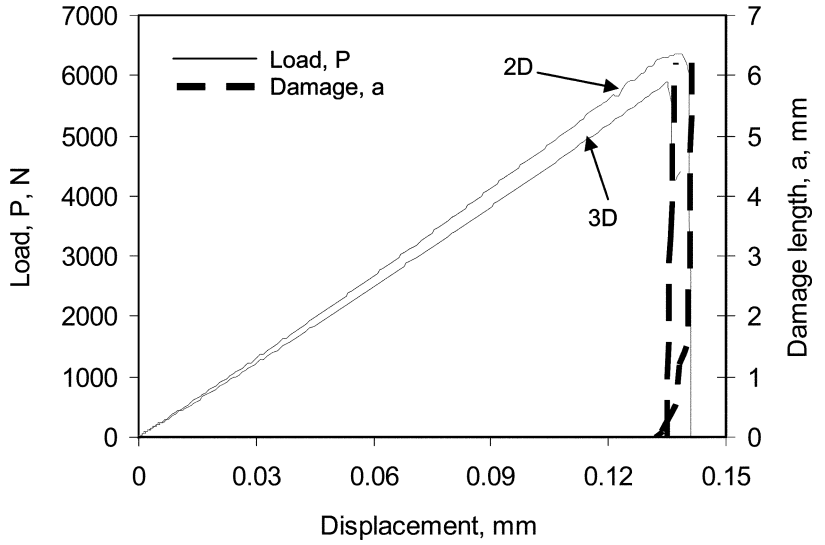

FIGURE 23 Predicted loading history and damage propagation in a 3D and 2D EA9321/aluminum SLJ model after exposure to a moist environment for 26 weeks (smallest mesh size 0.1 mm × 0.1 mm × 0.5 mm).

the 2D to the 3D model by about 5%. This is because more of the adhesive absorbs moisture and, hence, more of the adhesive has a reduced modulus, reducing the overall joint stiffness.

The damage propagation processes in the 2D and the 3D models are also shown in Figure 23. The damage propagation in the 3D model was much more rapid than the 2D model. These data, however, were taken from a section in the 3D model corresponding to the 2D model for the sake of comparison. To investigate the real spatial damage propagation in the 3D model, a series of contour plots are illustrated in Figure 24. The arrows in Figure 24 indicate the faces exposed to the environment. It is observed in combination with Figure 22 that the damage initiated around the corner of the joint at the saturated edge (A), rather than the slightly less degraded midplane section (B), and then propagated from the saturated corner to the middle (B) and the central section (C) of the adhesive layer rapidly. What is not clear from these figures is that failure also occurred in the lower layer of elements in the middle part of the joint. The edge of this is just visible as the white element faces around region (B) that first appear in Figure 24(b). It seemed that damage in the 3-direction was faster than in the 1-direction [see contour (b)]. Final failure occurred in the contour (d) after the load reached the ultimate resistance capacity of the joint.

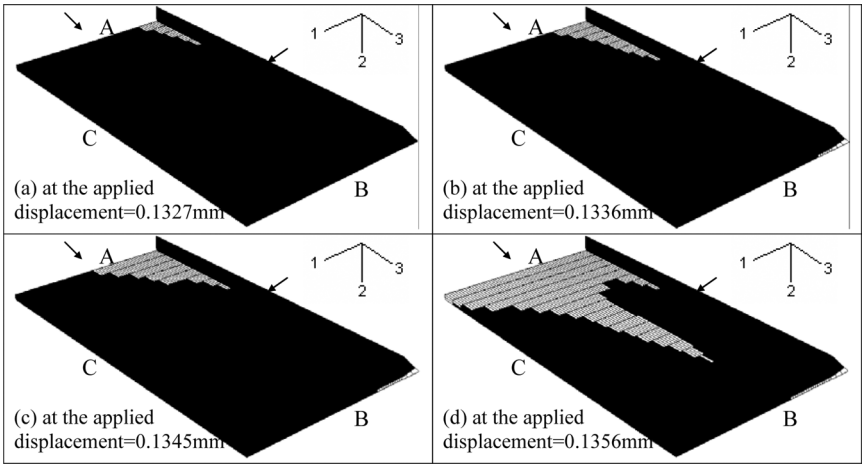

FIGURE 24 3D damage propagation in the EA9321/aluminum SLJ model (26 weeks degraded, smallest mesh size 0.1 mm × 0.1 mm × 0.5 mm).

Similar 3D analysis has been undertaken for the EA9321/composite single-lap joint using a 0.1 mm × 0.1 mm × 0.5 mm mesh refinement model, similar to that shown in Figure 21. The scheme with diffusion through the substrates and the same moisture-dependent critical strain were used in the modelling. The predicted loading history of

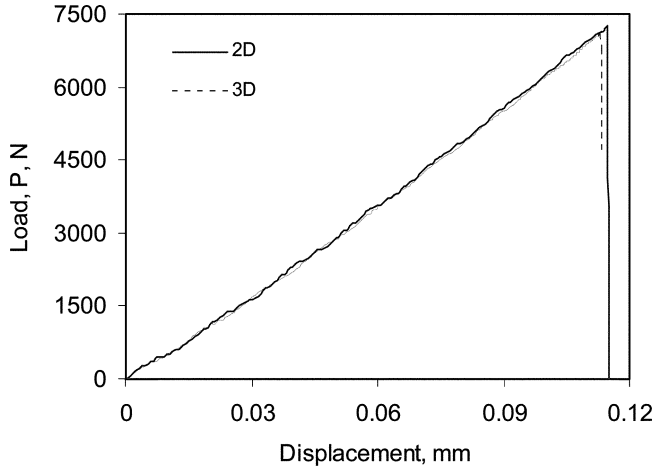

FIGURE 25 Predicted loading history in 3D and 2D EA9321/composite SLJ models after exposure to a moist environment for 26 weeks (smallest mesh size 0.1 mm × 0.1 mm × 0.5 mm).

the joint, exposed for a 26-week period, is shown in Figure 25. In this case, the predicted failure load and the joint stiffness for the 2D and 3D models were quite close. This can be explained because the orthotropic Young's modulus of the substrates is much higher (16 times) in the 1-direction than the other two directions, as shown in Table 2. Thus, adding the third dimension did not significantly change the structural response of the joint. Furthermore, at the longer exposure times the moisture mainly diffused through the substrates, and this was the same in both 2D and 3D cases. The damage propagation in the adhesive of the EA9321/composite joint has not been shown but was even faster than the EA9321/aluminum joint.

CONCLUSION

A strain-based cohesive failure model has been shown to model continuum failure successfully. A moisture-dependent critical strain was used to determine the residual strength of an adhesively bonded joint. A coupled diffusion-mechanical finite-element analysis was implemented using the commercial software package ABAQUS. A mixed-mode flexure test was used to calibrate this critical parameter by matching the numerical results with the associated experimental failure loads. The calibrated critical strain then was used to model failure in the other bonded joints with no further modification. EA9321-bonded aluminum and composite single-lap-joint specimens were selected to demonstrate the efficiency of the methodology. The numerical predictions for a range of degraded joints agree well with the corresponding experimental data. Another advantage of this method is the ability to predict and study the damage initiation and propagation during the loading. The problem of mesh dependence with this method was also successfully addressed. The method has then been extended to 3D modelling. An enhancement of the predicted damage initiation and propagation was obtained and discussed. For the configuration studied the enhancement was not significant, particularly for the composite bonded joints where diffusion through the composite was modelled in both 2D and 3D cases. It has been demonstrated that this methodology has much potential for use in predicting the residual strength of environmentally degraded adhesively bonded joints and also the damage or crack location and propagation.

ACKNOWLEDGEMENTS

The authors thank the Ministry of Defence for funding this work, David Liljedahl (University of Surrey) for experimental work on the

EA9321 adhesive and the MMF specimens, Terry Ackerman (MBDA) for experimental work on the lap joints, and Jeff Sargent (BAe Systems) for the composite diffusion measurements.

REFERENCES

[1] Beevers, A., *Int. J. Materials Product Technol*. **14**, 373–384 (1999).
[2] Loh, W. K., Crocombe, A. D., Abdel-Wahab, M. M., and Ashcroft, I. A., *Eng. Fract. Mechs.* **69**, 2113–2128 (2002).
[3] Loh, W. K., Crocombe, A. D., Abdel-Wahab, M. M., and Ashcroft, I. A., *J. Adhes.* **79**, 1135–1160 (2003).
[4] Liljedahl, C. D. M., Crocombe, A. D., Wahab, M. A., and Ashcroft, I. A., *J. Adhes. Sci. Tech.*, **19**, 525–548 (2005).
[5] Crocombe, A. D., Hua, Y. X., Loh, W. K., Wahab, M. A., and Ashcroft, I. A., *Int. J. Adhes. Adhesives*, **26**, 325–336 (2006).
[6] Gao, H., *J. Mech. Phys. Solids* **44**, 1453–1474 (1996).
[7] Zhang, P., Klein, P., Huang, Y., Gao, H., and Wu, P. D., *Comput. Model Engng. Sci.* **3**, 263–278 (2002).
[8] Thiagarajan, G., Hsia, K. J., and Huang, Y. Y., *Eng. Fract. Mech.* **71**, 401–423 (2004).
[9] Thiagarajan, G., Huang, Y. Y., and Hsia, K. J., *ASME J. Appl. Mech.* **71**, 796–804 (2004).
[10] Lee, E. H., *ASME J. Appl. Mech.* **36**, 1–6 (1969).
[11] Gurson, A. L., *J. Engrg. Mater. Technol.* **99**, 2–15 (1977).
[12] Chu, C. C. and Needleman, M., *J. Engng. Mater. Technol.* **102**, 249–256 (1980).
[13] Needleman, A. and Tvergaard, V., *J. Mech. Phys. Solids* **32**, 461–490 (1984).
[14] Needleman, A. and Tvergaard, V., *J. Mech. Phys. Solids* **35**, 151–183 (1987).
[15] Koplic, J. and Needleman, A., *Int. J. Solids Structures* **24**, 835–853 (1988).
[16] Reusch, F., Svendsen, B., and Klingbeil, D., *Eur. J. Mech. A/Solids* **22**, 779–792 (2003).
[17] Bonora, N., *J. Strain Anal. Eng. Des.* **34**, 463–478 (1999).
[18] Blocks, W., Klingbeil, D., Kunecke, G., and Sun, D. Z., *ASTM STP 1244*, M. Kirk and A. Bakker (Eds.) (American Society for Testing and Materials, Philadelphia, 1994).
[19] Lemaitre, J., *Engng. Fract. Mech.* **25**, 523–537 (1986).
[20] Lemaitre, J. and Chaboche, J. M., *Mechanics of Solid Materials* (Cambridge University Press, Cambridge, 1985).
[21] Bonora, N., *Engng. Fract. Mech.* **58**, 11–28 (1997).
[22] Crank, J., *The Mathematics of Diffusion,* 2nd ed (Oxford Science Publications, Oxford, 1975).
[23] ASTM E 104-85, *Standard Practice for Maintaining Constant Relative Humidity by Means of Aqueous Solutions* (American society for Testing and Materials, Philadelphia, 1991).
[24] Turkmen, H. S., Loge, R. E., Dawson, P. R., and Miller, M. P., *Int. J. Fatigue* **25**, 267–281 (2003).
[25] Schon, J., Nyman, T., Blom, A., and Ansell, H., *Compos. Sci. Technol.* **60**, 173–184 (2000).
[26] *ABAQUS/Explicit User's Manual* (HKS Inc, Pawtucket, RI, 2004), Version 6.4.